ELSEVIER

Journal of Fluids and Structures 26 (2010) 579–601

JOURNAL OF FLUIDS AND STRUCTURES

www.elsevier.com/locate/jfs

Numerical simulation of transonic limit cycle oscillations using high-order low-diffusion schemes

Baoyuan Wang, Ge-Cheng Zha*

Department of Mechanical and Aerospace Engineering, Miami Wind^{TM}, University of Miami, Coral Gables, FL 33124, USA

Received 6 February 2009; accepted 4 February 2010
Available online 3 April 2010

Abstract

This paper simulates the NLR7301 airfoil limit cycle oscillation (LCO) caused by fluid–structure interaction (FSI) using Reynolds averaged Navier–Stokes equations (RANS) coupled with Spalart–Allmaras (S–A) one-equation turbulence model. A low diffusion E-CUSP (LDE) scheme with 5th order weighted essentially nonoscillatory scheme (WENO) is employed to calculate the inviscid fluxes. A fully conservative 4th order central differencing is used for the viscous terms. A fully coupled fluid–structural interaction model is employed. For the case computed in this paper, the predicted LCO frequency, amplitudes, averaged lift and moment, all agree excellently with the experiment performed by Schewe et al. The solutions appear to have bifurcation and are dependent on the initial fields or initial perturbation. The developed computational fluid dynamics (CFD)/computational structure dynamics (CSD) simulation is able to capture the LCO with very small amplitudes measured in the experiment. This is attributed to the high order low diffusion schemes, fully coupled FSI model, and the turbulence model used. This research appears to be the first time that a numerical simulation of LCO matches the experiment. The simulation confirms several observations of the experiment.
© 2010 Elsevier Ltd. All rights reserved.

Keywords: Limited cycle oscillation; Fluid-structural interaction; High order scheme; WENO scheme

1. Introduction

Flow induced structural vibration is one of the most challenging problems affecting the military and commercial aircraft. Due to the complicated nonlinear fluid–structure interaction (FSI) phenomena, there is a lack of high fidelity computational tools to study the basic physics and to accurately predict structural failure. For the airframe, the FSI problems include transonic flutter, limit cycle oscillation, buzz, buffet, etc. For propulsion turbo-machinery, there are the problems such as high cycle fatigue caused by forced response or stall flutter, etc. Helicopter rotor blades constantly work under the vibration induced by blade wake and tip vortices. Recently, the growing interest of micro-air vehicles has posted many challengers in simulating FSI of flapping wings. The development of advanced methodologies to accurately simulate fluid–structure interactions hence will have broad impact on improving the performance of various aircraft.

The difficult issue that the FSI community has faced is the nonlinearity caused by both fluid and structure (Bendiksen and Seber, 2008). The aerodynamic nonlinearity poses more challenge than the structural one (Bendiksen, 1992; Tang

*Corresponding author. Tel.: +1 305 284 3328.
E-mail address: gzha@miami.edu (G.-C. Zha).

0889-9746/$ - see front matter © 2010 Elsevier Ltd. All rights reserved.
doi:10.1016/j.jfluidstructs.2010.02.003

Nomenclature

c_l, c_m	lift and moment coefficients, respectively
e	total energy per unit mass
$\mathbf{E}, \mathbf{F}, \mathbf{G}$	inviscid fluxes in ξ, η, ζ directions
h	plunge displacement
J	coordinates transformation Jacobian
M	Mach number
p	static pressure
Pr	Prandtl number
Pr_t	turbulent Prandtl number
r_α	radius of gyration
$\mathbf{R}, \mathbf{S}, \mathbf{T}$	viscous fluxes in ξ, η, ζ directions
Re	Reynolds number
t	time
u, v, w	Cartesian velocity components in x, y, z directions
x_α	static unbalance
x, y, z	Cartesian coordinates
α	pitching displacement
$\alpha(t)$	time dependent AoA
α_A	amplitude of the oscillating angle
α_m	mean value of the oscillating AoA
α_0	off-wind value of α
δ_h	Lehr heave damping
δ_α	Lehr pitching damping
μ	molecular viscosity in equations of flow; mass ratio in equations of motion
μ_t	turbulent viscosity
ν	kinematic viscosity
ξ, η, ζ	generalized coordinates
ρ	density
τ	molecular viscous stress tensor
ω	angular frequency
ω_α	uncoupled circular pitching frequency
ω_h	uncoupled circular heave frequency

et al., 2003). These problems are often accompanied or caused by complicated flow phenomena such as shock wave/turbulent boundary layer interaction, flow separation, vortex shedding, etc.

The transonic LCO is a challenging issue for numerical simulation due to the complex shock/boundary-layer interaction. The weak divergence, flutter divergence and onset of LCO could be captured and predicted quite well, but the amplitude of LCO was largely over-predicted by more than an order of magnitude for both the plunge and pitching amplitude. These can be seen in the work by Bendiksen (1992), Tang et al. (2003), Morton and Beran (1999) and Weber et al. (2001). Even though the inviscid Euler solver can capture the onset of LCO, the viscous Navier–Stokes solvers predict the LCO amplitude closer to experiments than the Euler solver. The LCO amplitude is also dependent on the turbulence model used as pointed out by Tang et al. (2003) when the NLR7301 airfoil is calculated (Schewe et al., 2003; Dietz et al., 2004). The nonlinear structural model does not really produce better results of LCO as indicated by Gordnier (2003). The calculation with wind tunnel wall porosity yields better LCO amplitude, but a significant difference remains if the actual wind tunnel wall porosity is used (Castro et al., 2001).

According to Bendiksen (1992), both the LCO and transonic dip may be caused by aerodynamic nonlinearity due to shock wave/turbulent boundary layer interaction and the resulted separation. Schewe et al. (2003) and Dietz et al. (2004) tend to support this hypothesis. Schewe et al. (2003) attribute two nonlinearity mechanisms to the amplitude-limiting phenomenon: (i) the oscillating shock strength and the coupled pulsations of the marginally separated flow beneath the shock; (ii) the trailing edge separation they deduced from the significant increase in the r.m.s. value of the pressure fluctuation near trailing edge.

Schewe et al. (2003) gave the following important observations and questions. First, the LCOs they captured have very small relative amplitudes of the plunge on the order of 2/1000 to 3/1000 of the chord and the pitching amplitude $<1^\circ$. They questioned if the LCOs of such small amplitudes are the artifacts of the wind-tunnel experiment or could also occur in unbounded flow. Second, since all the reported numerical simulations at that time only captured the much greater LCO amplitudes, they questioned if it means the co-existence of multiple LCOs at constant flow conditions. They discovered the multiple coexisting LCOs in their experiments. Third, they found that the wall boundary layer transition from laminar to turbulent does not have much effect on LCO. Fourth, they verified that the wind tunnel wall interference with or without perforated test-section does not have much effect on LCOs. Fifth, they observed that the transition from steady to oscillatory state can be either continuous or discontinuous.

Most of the calculations of fluid–structure interaction today employ 2nd order accuracy in both space and time. The shock wave/boundary layer interaction is considered as the critical factor affecting the nonlinearity of transonic airfoil LCO (Schewe et al., 2003). It is hence very important to have a high-resolution low-diffusion shock capturing scheme to resolve shock/boundary-layer interaction. The WENO scheme is a desirable candidate since it can achieve uniformly high order accuracy up to the shock discontinuities. In addition, the low diffusion of the numerical scheme is important to accurately predict flow damping, which may significantly affect the structure displacement.

The objective of this research is to simulate the challenging nonlinear LCO phenomenon with high fidelity numerical algorithms, which include the high order (5th order) WENO scheme (Shu, 1997; Shen et al., 2007), a low diffusion

E-CUSP (LDE) Riemann solver (Zha et al., 2008; Wang and Zha, 2008a), a new 4th order fully conservative central differencing scheme for viscous terms (Shen et al., 2007), an implicit 2nd order accuracy time marching scheme with Gauss–Seidel line relaxation, a fully coupled fluid–structural interaction model (Chen et al., 2004, 2007; Chen and Zha, 2005), and advanced Spalart–Allmaras (S–A) one-equation RANS turbulence model (Spalart and Allmaras, 1992).

The rigorous algorithm of this research appears to have paid off, with the numerical simulation matching the experiment excellently for the first time. This simulation also confirms some of the experimental observations and answers some important questions. First, the LCOs with the small relative amplitude is captured with unbounded flows in the numerical simulation. This means they should not be the artifacts of the wind-tunnel experiment and most likely are a factual phenomenon. Second, the co-existence of multiple LCOs at constant flow conditions is confirmed in our simulation. The reason that other numerical simulations only capture the LCOs with large amplitudes may be due to their high numerical dissipation that either smears out the small amplitude LCO or is only able to resolve the large amplitudes LCOs. Third, the numerical simulation of this research confirms that the wall boundary layer transition from laminar to turbulent does not have a large effect on LCOs at high Reynolds number, because our simulation assumes that the boundary layer is fully turbulent from the airfoil leading edge. Fourth, the simulation confirms that the wind tunnel wall interference with or without perforated test-section does not have much effect on LCOs, because our simulation uses the unbounded flow condition with no wind tunnel wall effect at all. Fifth, the numerically captured LCO is accompanied with a very small flow separation near the trailing edge, which is consistent with the speculation of Schewe et al. (2003) obtained from the experiment. This verifies the hypothesis that the LCO processes are maintained by the nonlinearity of flow separation induced by shock/boundary-layer interaction.

2. Governing equations

The governing equations are the Reynolds Averaged Navier–Stokes (RANS) equations coupled with the Spalart–Allmaras (S–A) one-equation turbulence model (Spalart and Allmaras, 1992). In a generalized coordinate system, the conservative form of the equations are given as the following:

$$\frac{\partial Q}{\partial t}+\frac{\partial \mathbf{E}}{\partial \xi}+\frac{\partial \mathbf{F}}{\partial \eta}+\frac{\partial \mathbf{G}}{\partial \zeta}=\frac{1}{\mathrm{Re}}\left(\frac{\partial \mathbf{R}}{\partial \xi}+\frac{\partial \mathbf{S}}{\partial \eta}+\frac{\partial \mathbf{T}}{\partial \zeta}+\mathbf{D}\right), \tag{1}$$

where

$$Q=\frac{1}{\mathrm{J}}\begin{Bmatrix}\rho\\ \rho u\\ \rho v\\ \rho w\\ \rho e\\ \rho\tilde{\nu}\end{Bmatrix}, \tag{2}$$

$$\mathbf{E}=\begin{Bmatrix}\rho U\\ \rho uU+l_x p\\ \rho vU+l_y p\\ \rho wU+l_z p\\ (\rho e+p)U-l_t p\\ \rho\tilde{\nu}U\end{Bmatrix},\quad \mathbf{F}=\begin{Bmatrix}\rho V\\ \rho uV+m_x p\\ \rho vV+m_y p\\ \rho wV+m_z p\\ (\rho e+p)V-m_t p\\ \rho\tilde{\nu}V\end{Bmatrix},\quad \mathbf{G}=\begin{Bmatrix}\rho W\\ \rho uW+n_x p\\ \rho vW+n_y p\\ \rho wW+n_z p\\ (\rho e+p)W-n_t p\\ \rho\tilde{\nu}W\end{Bmatrix}, \tag{3}$$

$$\mathbf{R}=\begin{Bmatrix}0\\ l_k\tau_{xk}\\ l_k\tau_{yk}\\ l_k\tau_{zk}\\ l_k\beta_k\\ \frac{\rho}{\sigma}(\nu+\tilde{\nu})(\mathbf{l}\cdot\nabla\tilde{\nu})\end{Bmatrix},\quad \mathbf{S}=\begin{Bmatrix}0\\ m_k\tau_{xk}\\ m_k\tau_{yk}\\ m_k\tau_{zk}\\ m_k\beta_k\\ \frac{\rho}{\sigma}(\nu+\tilde{\nu})(\mathbf{m}\cdot\nabla\tilde{\nu})\end{Bmatrix},\quad \mathbf{T}=\begin{Bmatrix}0\\ n_k\tau_{xk}\\ n_k\tau_{yk}\\ n_k\tau_{zk}\\ n_k\beta_k\\ \frac{\rho}{\sigma}(\nu+\tilde{\nu})(\mathbf{n}\cdot\nabla\tilde{\nu})\end{Bmatrix}, \tag{4}$$

$$D=\frac{1}{\mathrm{J}}\begin{Bmatrix}0\\0\\0\\0\\0\\S_v\end{Bmatrix}, \tag{5}$$

where

$$\beta_k=u_i\tau_{ki}-q_k, \tag{6}$$

$$S_v=\rho C_{b1}(1-f_{t2})\tilde{S}\tilde{v}+\frac{1}{\mathrm{Re}}\left[-\rho\left(C_{w1}f_w-\frac{C_{b1}}{\kappa^2}f_{t2}\right)\left(\frac{\tilde{v}}{d}\right)^2+\frac{\rho}{\sigma}C_{b2}(\nabla\tilde{v})^2-\frac{1}{\sigma}(v+\tilde{v})\nabla\tilde{v}\cdot\nabla\rho\right]+\mathrm{Re}[\rho f_{t1}(\Delta U)^2]. \tag{7}$$

In the equations above, U, V and W are the contravariant velocities in ξ, η and ζ directions.

$$U=l_t+\mathbf{l}\cdot\mathbf{V}=l_t+l_xu+l_yv+l_zw,$$

$$V=m_t+\mathbf{m}\cdot\mathbf{V}=m_t+m_xu+m_yv+m_zw,$$

$$W=n_t+\mathbf{n}\cdot\mathbf{V}=n_t+n_xu+n_yv+n_zw, \tag{8}$$

where $\mathbf{V}=(u,v,w)$ is the velocity vector, $\mathbf{l},\mathbf{m},\mathbf{n}$ are the normal vectors on ξ,η,ζ surfaces with their magnitudes equal to the elemental surface area and pointing to the directions of increasing ξ,η,ζ,

$$\mathbf{l}=\frac{\nabla\xi}{\mathrm{J}}\,\mathrm{d}\eta\,\mathrm{d}\zeta,\quad \mathbf{m}=\frac{\nabla\eta}{\mathrm{J}}\,\mathrm{d}\xi\,\mathrm{d}\zeta,\quad \mathbf{n}=\frac{\nabla\zeta}{\mathrm{J}}\,\mathrm{d}\xi\,\mathrm{d}\eta; \tag{9}$$

l_t, m_t, n_t stand for the grid moving velocities and are defined as

$$l_t=\frac{\xi_t}{\mathrm{J}}\,\mathrm{d}\eta\,\mathrm{d}\zeta,\quad m_t=\frac{\eta_t}{\mathrm{J}}\,\mathrm{d}\xi\,\mathrm{d}\zeta,\quad n_t=\frac{\zeta_t}{\mathrm{J}}\,\mathrm{d}\xi\,\mathrm{d}\eta. \tag{10}$$

When the grid is stationary, $l_t=m_t=z_t=0$.

Since $\Delta\xi=\Delta\eta=\Delta\zeta=1$ are used in the current discretization, Eqs. (9) and (10) are written as follows in the solver:

$$\mathbf{l}=\frac{\nabla\xi}{\mathrm{J}},\quad \mathbf{m}=\frac{\nabla\eta}{\mathrm{J}},\quad \mathbf{n}=\frac{\nabla\zeta}{\mathrm{J}}, \tag{11}$$

$$l_t=\frac{\xi_t}{\mathrm{J}},\quad m_t=\frac{\eta_t}{\mathrm{J}},\quad n_t=\frac{\zeta_t}{\mathrm{J}}. \tag{12}$$

The shear-stress τ_{ik} and total heat flux q_k in Cartesian coordinates can be expressed as

$$\tau_{ik}=(\mu+\mu_t)\left[\left(\frac{\partial u_i}{\partial x_k}+\frac{\partial u_k}{\partial x_i}\right)-\frac{2}{3}\delta_{ik}\frac{\partial u_j}{\partial x_j}\right], \tag{13}$$

$$q_k=-\left(\frac{\mu}{\mathrm{Pr}}+\frac{\mu_t}{\mathrm{Pr}_t}\right)\frac{\partial T}{\partial x_k}, \tag{14}$$

where Pr is the Prandtl number, Pr_t is the turbulent Prandtl number, μ is the molecular viscosity determined by Sutherland law, and μ_t is the turbulent viscosity determined by the S–A model (Spalart and Allmaras, 1992),

$$\mu_t=\rho\tilde{v}f_{v1}. \tag{15}$$

The kinematic viscosity v is defined as

$$v=\frac{\mu}{\rho}. \tag{16}$$

In Eqs. (4), (6), (13) and (14), the repeated subscripts i or k represent the coordinates x, y and z, following the Einstein summation convention. Eqs. (13) and (14) will be transformed to a generalized coordinate system in computation.

The sixth equation of the governing Eqs. (1)–(5) is the S–A one-equation turbulence model (Spalart and Allmaras, 1992). The functions in the equation are given as

$$f_{v1}=\frac{\chi^3}{\chi^3+C_{v1}^3},\quad \chi=\frac{\tilde{\nu}}{\nu},$$

$$\tilde{S}=S+\frac{\tilde{\nu}}{\mathrm{Re}\,\kappa^2 \mathrm{d}^2}f_{v2},\quad f_{v2}=1-\frac{\chi}{1+\chi f_{v1}},$$

$$f_w=g\left[\frac{1+C_{w3}^6}{g^6+C_{w3}^6}\right]^{1/6},\quad g=r+C_{w2}\left(r^6-r\right),\quad r=\frac{\tilde{\nu}}{\mathrm{Re}\,\tilde{S}\kappa^2 \mathrm{d}^2},$$

$$f_{t1}=C_{t1}g_t\exp\left[-C_{t2}\frac{\omega_t^2}{\Delta U^2}(d^2+g_t^2 d_t^2)\right],\quad g_t=\min\left(0.1,\frac{\Delta U}{\omega_t \Delta x_t}\right),$$

$$f_{t2}=C_{t3}\exp(-C_{t4}\chi^2), \tag{17}$$

where

$$S=\sqrt{\left(\frac{\partial w}{\partial y}-\frac{\partial v}{\partial z}\right)^2+\left(\frac{\partial u}{\partial z}-\frac{\partial w}{\partial x}\right)^2+\left(\frac{\partial v}{\partial x}-\frac{\partial u}{\partial y}\right)^2}$$

is the magnitude of vorticity, which is also transformed to generalized coordinate system, ω_t is the wall vorticity at the wall boundary layer trip location, d is the distance to the closest wall. d_t is the distance of the field point to the trip location, ΔU is the difference of the velocities between the field point and the trip location, Δx_t is the grid spacing along the wall at the trip location.

The constants in S–A model are set to have the following values:

$$\sigma=\tfrac{2}{3},\quad C_{b1}=0.1355,\quad C_{b2}=0.622,\quad \kappa=0.41,\quad C_{v1}=7.1,$$

$$C_{w1}=C_{b1}/\kappa^2+(1+C_{b2})/\sigma,\quad C_{w2}=0.3,\quad C_{w3}=2,$$

$$C_{t1}=1,\quad C_{t2}=2,\quad C_{t3}=1.2,\quad C_{t4}=0.5.$$

For large r, f_w reaches a constant. So, if $r\geq 10$, we let $r=10$.

The initial value and boundary conditions of $\tilde{\nu}$ are given as the following (Wang and Zha, 2008a):

initial value :	$\tilde{\nu}=2$,
at walls :	$\tilde{\nu}=0$,
far field inflow :	$\tilde{\nu}=0.02$,
far field outflow :	$\tilde{\nu}$ is extrapolated.

3. The numerical method

3.1. The low-diffusion E-CUSP (LDE) scheme

The LDE scheme developed by Zha et al. (2008) is employed to evaluate the inviscid fluxes. The basic idea of the LDE scheme is to split the inviscid flux into the convective flux E^c and the pressure flux E^p. Even with the one extra

equation from the S–A model, the splitting is basically the same as the original scheme for the Euler equation and is straightforward. This is an advantage over the Roe scheme, for which the eigenvectors need to be derived when any extra equation is added to the governing equations.

In generalized coordinate system, the flux **E** can be split as follows:

$$\mathbf{E} = E^c + E^p = \begin{Bmatrix} \rho U \\ \rho u U \\ \rho v U \\ \rho w U \\ \rho e U \\ \rho \tilde{v} U \\ \\ \end{Bmatrix} + \begin{Bmatrix} 0 \\ l_x p \\ l_y p \\ l_z p \\ p\overline{U} \\ 0 \\ \\ \end{Bmatrix}, \tag{18}$$

where U is the contravariant velocity in ξ direction and is defined as

$$U = l_t + l_x u + l_y v + l_z w; \tag{19}$$

$\overline{U}$ is defined as

$$\overline{U} = l_x u + l_y v + l_z w. \tag{20}$$

The convective term, E^c is evaluated by

$$E^c = \rho U \begin{Bmatrix} 1 \\ u \\ v \\ w \\ e \\ \tilde{v} \\ \\ \end{Bmatrix} = \rho U f^c, \quad f^c = \begin{Bmatrix} 1 \\ u \\ v \\ w \\ e \\ \tilde{v} \\ \\ \end{Bmatrix}. \tag{21}$$

Let

$$C = c(l_x^2 + l_y^2 + l_z^2)^{1/2}, \tag{22}$$

where $c = \sqrt{\gamma RT}$ is the speed of sound. Then the convective flux at interface $i + \frac{1}{2}$ is evaluated as

$$E^c_{i+1/2} = C_{1/2}[\rho_L C^+ f^c_L + \rho_R C^- f^c_R], \tag{23}$$

where the subscripts L and R represent the left- and right-hand sides of the interface, and

$$C_{1/2} = \tfrac{1}{2}(C_L + C_R), \quad C^+ = \alpha^+_L(1+\beta_L)M_L - \beta_L M^+_L - M^+_{1/2}, \quad C^- = \alpha^-_R(1+\beta_R)M_R - \beta_R M^-_R + M^-_{1/2},$$

$$M_L = \frac{U_L}{C_{1/2}}, \quad M_R = \frac{U_R}{C_{1/2}}, \quad \alpha_{L,R} = \frac{1}{2}[1 \pm \mathrm{sign}(M_{L,R})], \quad \beta_{L,R} = -\max[0, 1 - \mathrm{int}(|M_{L,R}|)],$$

$$M^+_{1/2} = M_{1/2}\frac{C_R + C_L\Phi}{C_R + C_L}, \quad M^-_{1/2} = M_{1/2}\frac{C_L + C_R\Phi^{-1}}{C_R + C_L}, \quad \Phi = \frac{(\rho C^2)_R}{(\rho C^2)_L},$$

$$M_{1/2} = \beta_L \delta^+ M^-_L - \beta_R \delta^- M^+_R, \quad M^\pm_{L,R} = \pm\tfrac{1}{4}(M_{L,R} \pm 1)^2, \quad \delta^\pm = \tfrac{1}{2}\{1 \pm \mathrm{sign}[\tfrac{1}{2}(M_L + M_R)]\}.$$

The pressure flux, E^p is evaluated as follows:

$$E^p_{i+1/2} = \begin{Bmatrix} 0 \\ \mathcal{P}^+ pl_x \\ \mathcal{P}^+ pl_y \\ \mathcal{P}^+ pl_z \\ \frac{1}{2}p[\overline{U} + \overline{C}_{1/2}] \\ 0 \end{Bmatrix}_L + \begin{Bmatrix} 0 \\ \mathcal{P}^- pl_x \\ \mathcal{P}^- pl_y \\ \mathcal{P}^- pl_z \\ \frac{1}{2}p[\overline{U} - \overline{C}_{1/2}] \\ 0 \end{Bmatrix}_R . \tag{24}$$

The contravariant speed of sound $\overline{C}$ in the pressure vector is consistent with $\overline{U}$. It is computed based on C as

$$\overline{C} = C - l_t. \tag{25}$$

The use of $\overline{U}$ and $\overline{C}$ instead of U and C in the pressure term of the energy equation is to take into account the grid speed, so that the flux will transit from subsonic to supersonic smoothly. When the grid is stationary, $l_t = 0$, $\overline{C} = C$, $\overline{U} = U$.

The pressure splitting coefficient is

$$\mathcal{P}^{\pm}_{L,R} = \tfrac{1}{4}(M_{L,R} \pm 1)^2(2 \mp M_L). \tag{26}$$

3.2. The fifth-order WENO scheme

The interface flux, $E_{i+1/2} = E(Q_L, Q_R)$, is evaluated by determining the conservative variables Q_L and Q_R using the fifth-order finite difference WENO scheme (Shen et al., 2007, 2009). For example

$$(Q_L)_{i+1/2} = \omega_0 q_0 + \omega_1 q_1 + \omega_2 q_2, \tag{27}$$

where

$$q_0 = \tfrac{1}{3}Q_{i-2} - \tfrac{7}{6}Q_{i-1} + \tfrac{11}{6}Q_i, \quad q_1 = -\tfrac{1}{6}Q_{i-1} + \tfrac{5}{6}Q_i + \tfrac{1}{3}Q_{i+1}, \quad q_2 = \tfrac{1}{3}Q_i + \tfrac{5}{6}Q_{i+1} - \tfrac{1}{6}Q_{i+2}, \tag{28}$$

$$\omega_k = \frac{\alpha_k}{\alpha_0 + \cdots + \alpha_{r-1}}, \tag{29}$$

$$\alpha_k = \frac{C_k}{\varepsilon + IS_k}, \quad k = 0, \ldots, r-1, \tag{30}$$

$$C_0 = 0.1, \quad C_1 = 0.6, \quad C_2 = 0.3, \tag{31}$$

$$IS_0 = \tfrac{13}{12}(Q_{i-2} - 2Q_{i-1} + Q_i)^2 + \tfrac{1}{4}(Q_{i-2} - 4Q_{i-1} + 3Q_i)^2,$$

$$IS_1 = \tfrac{13}{12}(Q_{i-1} - 2Q_i + Q_{i+1})^2 + \tfrac{1}{4}(Q_{i-1} - Q_{i+1})^2,$$

$$IS_2 = \tfrac{13}{12}(Q_i - 2Q_{i+1} + Q_{i+2})^2 + \tfrac{1}{4}(3Q_i - 4Q_{i+1} + Q_{i+2})^2, \tag{32}$$

where ε in Eq. (30) is originally introduced to avoid the denominator becoming zero and is supposed to be a very small number. In Shen et al. (2007, 2009), it is observed that IS_k will oscillate if ε is too small and also shift the weights away from the optimum values in the smooth region. The higher the ε values, the closer the weights approach the optimum weights, C_k, which will give the symmetric evaluation of the interface flux with minimum numerical dissipation. When there are shocks in the flow field, ε cannot be too large to maintain the sensitivity to shocks. In Shen et al. (2007, 2009), $\varepsilon = 10^{-2}$ is recommended for transonic flows with shock waves.

The viscous terms are discretized by a fully conservative fourth-order accurate finite central differencing scheme developed by Shen et al. (2007, 2008).

3.3. Implicit time integration

The time dependent governing equations are solved using dual time stepping method suggested by Jameson (1991). To achieve a high convergence rate, the implicit pseudo time marching scheme is used with the unfactored Gauss–Seidel line relaxation. The physical temporal term is discretized implicitly using a three point, backward differencing as in the following:

$$\frac{\partial Q}{\partial t}=\frac{3Q^{n+1}-4Q^{n}+Q^{n-1}}{2\Delta t}, \tag{33}$$

where $n-1$, n and $n+1$ are three sequential time levels, which have a time interval of Δt. The first-order Euler scheme is used to discretize the pseudo temporal term. The semi-discretized equations of the governing equations are finally given as follows:

$$\left[\left(\frac{1}{\Delta\tau}+\frac{1.5}{\Delta t}\right)I-\left(\frac{\partial R}{\partial Q}\right)^{n+1,m}\right]\delta Q^{n+1,m+1}=R^{n+1,m}-\frac{3Q^{n+1,m}-4Q^{n}+Q^{n-1}}{2\Delta t}, \tag{34}$$

where $\Delta\tau$ is the pseudo time step, R is the net flux evaluated on a grid point using the fifth-order finite difference WENO scheme for the inviscid fluxes and the fourth-order central differencing scheme for the viscous terms (Shen et al., 2007, 2009, 2008).

4. Equations of motion

The NLR7301 airfoil is elastically mounted as shown in Fig. 1. The nondimensional form of the equations governing the motion of the two-degree-of-freedom spring-mass-damper system are

$$\begin{pmatrix}1 & -x_\alpha\\ -x_\alpha & r_\alpha^2\end{pmatrix}\frac{\partial^2 q}{\partial t^2}+2\begin{pmatrix}\delta_h\omega_h & 0\\ 0 & r_\alpha^2\delta_\alpha\omega_\alpha\end{pmatrix}\frac{\partial q}{\partial t}+\begin{pmatrix}\omega_h^2 & 0\\ 0 & r_\alpha^2\omega_\alpha^2\end{pmatrix}q=\frac{2}{\pi\mu}\begin{pmatrix}c_l\\ c_m\end{pmatrix}, \tag{35}$$

where x_α is the static unbalance, r_α is radius of gyration, ω_α is uncoupled circular pitching frequency, ω_h is uncoupled circular heave frequency, δ_α is Lehr pitching damping, δ_h is Lehr heave damping, μ is mass ratio, c_l and c_m are lift and moment coefficients, respectively. q is defined by

$$q=\begin{pmatrix}q_1\\ q_2\end{pmatrix}=\begin{pmatrix}h\\ \alpha-\alpha_0\end{pmatrix}, \tag{36}$$

in which h and α are the plunge and pitching displacements, respectively, α_0 is the off-wind value of α.

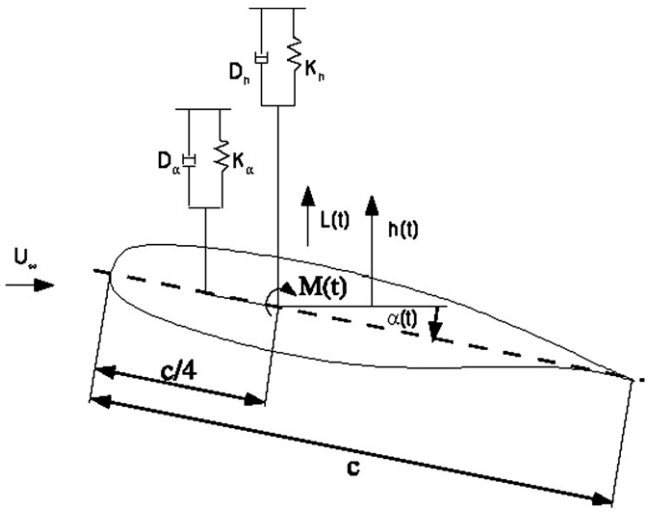

Fig. 1. Model of the elastically mounted NLR7301 airfoil.

Eq. (35) is transformed to a state matrix form and expressed as

$$M\frac{\partial S}{\partial t}+K\cdot S=Q, \tag{37}$$

where

$$S=\begin{Bmatrix} q_1 \\ \dfrac{\partial q_1}{\partial t} \\ q_2 \\ \dfrac{\partial q_2}{\partial t} \end{Bmatrix},\quad M=\begin{Bmatrix} 1 & 0 & 0 & 0 \\ 0 & 1 & 0 & -x_\alpha \\ 0 & 0 & 1 & 0 \\ 0 & -x_\alpha & 0 & r_\alpha^2 \end{Bmatrix},\quad K=\begin{Bmatrix} 0 & -1 & 0 & 0 \\ \omega_h^2 & 2\delta_h\omega_h & 0 & 0 \\ 0 & 0 & 0 & -1 \\ 0 & 0 & r_\alpha^2\omega_\alpha^2 & 2r_\alpha^2\delta_\alpha\omega_\alpha \end{Bmatrix},\quad Q=\begin{Bmatrix} 0 \\ \dfrac{2}{\pi\mu}c_l \\ 0 \\ \dfrac{2}{\pi\mu}c_m \end{Bmatrix}.$$

The structural equation (37) is discretized and solved implicitly in each physical time step in a manner consistent with flow governing equations (34):

$$\left(\frac{1}{\Delta\tau}I+\frac{1.5}{\Delta t}M+K\right)\delta S^{n+1,m+1}=Q^{n+1,m+1}-M\frac{3S^{n+1,m}-4S^n+S^{n-1}}{2\Delta t}-KS^{n+1,m}. \tag{38}$$

The fluid–structure interaction is implemented in a fully couple manner (Chen et al., 2004, 2007; Chen and Zha, 2005). Within each physical time step, the flow equations and structural equations are iterated simultaneously until the prescribed convergence criteria are satisfied for both flow and structural solver. After the convergence criteria are reached with the max-Norm residual smaller than 10^{-6}, the fluid–structural interaction proceeds to the next physical time step.

5. Results and discussion

The algorithm is first validated with experiment for the forced pitching airfoil, NACA64A010, and then is used to calculate the LCO of NLR7301 Airfoil.

5.1. Forced pitching airfoil

As a validation case of transonic airfoil fluid–structure interaction, a forced pitching airfoil, NACA64A010 is calculated and the results are compared with experiment.

For this transonic airfoil, an O-type grid is generated with the dimension of 281×66 (see Fig. 2).

The airfoil is forced in pitch about its quarter chord sinusoidally. The airfoil oscillation is defined by a function of the time-dependent angle of attack (AoA):

$$\alpha(t)=\alpha_m+\alpha_A\sin(\omega t), \tag{39}$$

where $\alpha(t)$ is the time dependent AoA, α_m is the mean value of the oscillating AoA, α_A is the amplitude of the oscillating angle, ω is the angular frequency which is directly related to the reduced frequency

$$k_c=\frac{\omega C}{2U_\infty}, \tag{40}$$

where C is the chord of the airfoil, and U_∞ is the free-stream velocity.

To be consistent with the experiment, the following primary parameters are employed in the unsteady calculation: $\alpha_m=0$, $\alpha_A=1.01^\circ$, Reynolds number (based on chord), $\mathrm{Re}=1.256\times 10^7$, free-stream Mach number, $M_\infty=0.8$, and reduced frequency, $k_c=0.202$. The computation begins with a uniform flow field of free stream at $\alpha=0^\circ$. The dimensionless time step is $\Delta t=0.05$.

Fig. 3 shows the lift coefficients varying with the AoA after the flow field reaches its temporally periodic solution. The computed lift coefficients agree well with the experiment of Davis (1982). Fig. 4 shows the moment coefficients varying with the AoA. The agreement of the moment coefficient is not as good as that of the lift coefficient. However, the agreement in the current results is better than the results computed by McMullen et al. (2002). The discrepancy between computation and experiment in the moment coefficient is not fully understood.

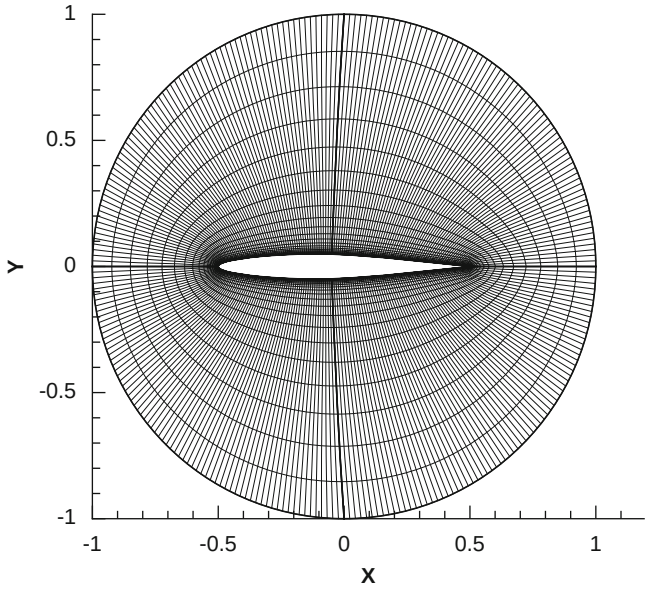

Fig. 2. The computational grid of NACA64A010 airfoil.

5.2. LCO of NLR7301 airfoil

The LCO case simulated is the test case No. 77 (Schewe et al., 2002, 2003; Dietz et al., 2004) of NLR7301 airfoil. The chord length of the airfoil is 0.3 m and the mean angle of attack is 1.28°. The experimental conditions are the free-stream Mach number of 0.768 and the Reynolds number of 1.727×10^6 based on the chord length.

The nondimensional structural parameters used for the computation of fluid–structure interaction are summarized in Table 1.

There exists always some discrepancy between the experiment and numerical simulation, which may result from experimental and numerical uncertainties. In addition, it is observed that the LCOs are sensitive to initial conditions due to bifurcation phenomenon. It is thus difficult to match the numerical initial perturbations with those in the experiment. That is, if we directly use the experimental conditions only, the results may not match the experiment well, or could be totally different. The numerical simulation hence involves a search process to match the experimental conditions and results as much as possible.

In our numerical simulation, it is observed that the primary factors affecting LCO are Mach number, AoA and α_0. The present study investigates the effect of these factors and searches the values that the computed LCO agrees best with the experiment. Two different procedures are conducted to simulate the LCO.

Procedure 1 follows the criterion used by Weber et al. (2001) and Tang et al. (2003), in which, both Mach number and AoA are adjusted to match steady state surface pressure distribution between computation and experiment as much as possible. The obtained Mach number and AoA are then fixed in the LCO simulation by adjusting the α_0 until the computed time-averaged AoA is close to the obtained AoA of the steady state computation.

Procedure 2 is developed in this research, in which the Mach number is fixed and the α_0 as well as initial AoA are iterated to match the experimental LCO amplitudes. The resulting time-averaged lift and moment are also taken into account to compare with the experiment.

All simulations are conducted on an MPI based computer cluster with parallel computation. The parallel computation is performed by a high efficiency algorithm with a general mapping procedure developed for multi-block structured grid CFD methods (Wang and Zha, 2008b).

5.2.1. Steady state flow computation

The baseline grid is a single block O-type grid with dimension of 193×97 and is equally partitioned into 16 sub-blocks with 8 blocks in the circumferential direction and two blocks in radial direction as shown in Fig. 5. The mesh dimension of each sub-block is 25×49.

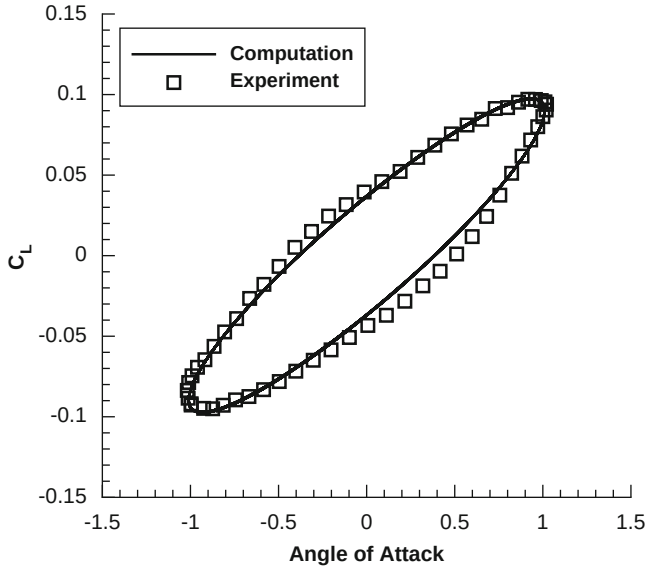

Fig. 3. Comparison of computed lift coefficient with experimental data for the forced pitching airfoil.

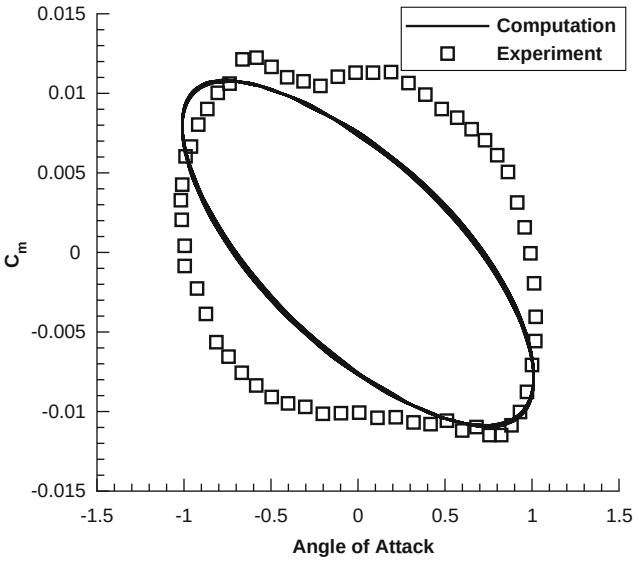

Fig. 4. Comparison of computed moment coefficient with experimental data for the forced pitching airfoil.

Table 1
The nondimensional structural parameters used for computation.

Mach number	x_α	r_α	δ_α	δ_h	μ	ω_α	ω_h
0.768	0.0484	0.197	0.0041	0.0073	942	0.31988	0.24306
0.753	0.0484	0.197	0.0041	0.0073	942	0.32625	0.24790

The steady-state computations are conducted first to search for the flow conditions that match the computed pressure distribution best with the experiment. Both the widely used Mach number, M, of 0.753 for CFD (Weber et al., 2001; Tang et al., 2003) and the experimental Mach number of 0.768 are simulated. It is found that the steady state surface

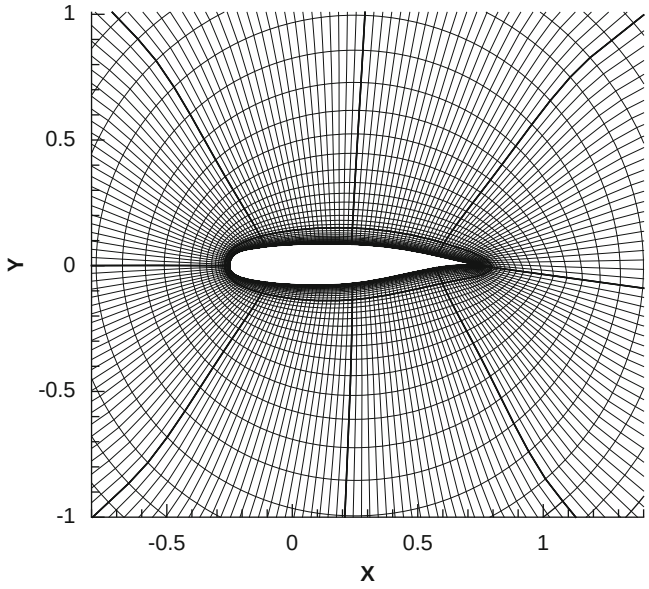

Fig. 5. The computational grid of NLR7301 airfoil.

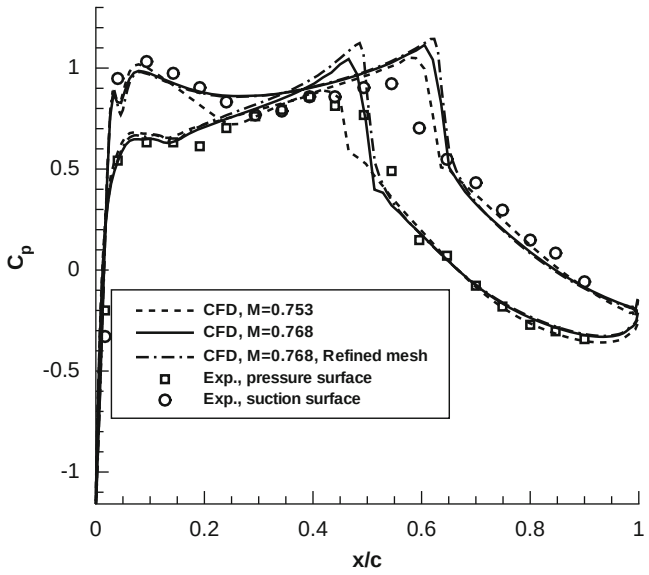

Fig. 6. Steady state pressure coefficient distribution on the surface of NLR7301 airfoil.

pressure agrees best with experiment at $AoA = -0.45^\circ$ for M = 0.753 and at $AoA = -0.2^\circ$ for M = 0.768. However, both cases have some discrepancy with the experiment. Fig. 6 shows the surface pressure distribution for the two cases. For the case of M = 0.753, the shock location at the suction surface agrees better with the experiment, whereas for M = 0.768, the shock location at the pressure surface agrees better. Overall, the computed case with the experimental M = 0.768 is closer to experiment upstream and downstream of the shocks.

Mesh refinement is performed for the steady state case at Mach number M = 0.768 to confirm that the baseline mesh is sufficient to be used for unsteady LCO simulation. The baseline mesh is refined in both directions with the mesh size increased by four times to 385×193. As shown in Fig. 6, the computed surface pressure distributions between the baseline and refined mesh have little difference, except that the refined mesh has sharper shock profile due to the denser mesh.

5.2.2. LCO simulation

5.2.2.1. Mach number=0.753. The first series of LCO search uses procedure 1 at M = 0.753 and $AoA = -0.45^\circ$, which are the conditions used by the research groups of Weber et al. (2001) and Tang et al. (2003). The LCO computation is conducted by adjusting α_0, the off-wind value of α to make the time-averaged AoA agree with $AoA = -0.45^\circ$. The LCO computation is conducted using two different initial flow fields to investigate the effects of initial flow and perturbation. One initial field is the solution of the steady-state computation. The other initial field is the uniform free-stream flow. Both LCO computations start at $AoA = 0^\circ$. The dimensionless time step of 0.01 is used. The dimensionless time is defined as $t_c = t/(c/u_\infty)$, where t is the physical time.

The convergence history within a typical physical time step is shown in Fig. 7 at Mach number of 0.753 and α_0 of 0.25°. Figs. 8 and 9 show the computed LCO amplitudes. Both initial fields predict the final LCOs with about the same

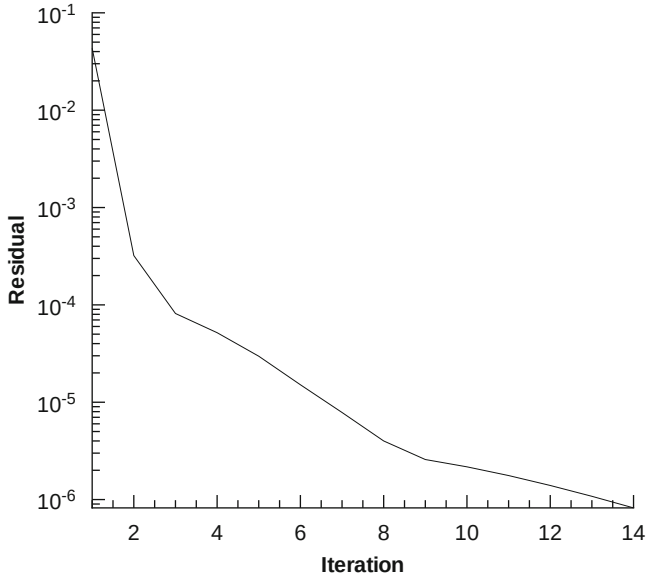

Fig. 7. Convergence history within a typical physical time step for M = 0.753.

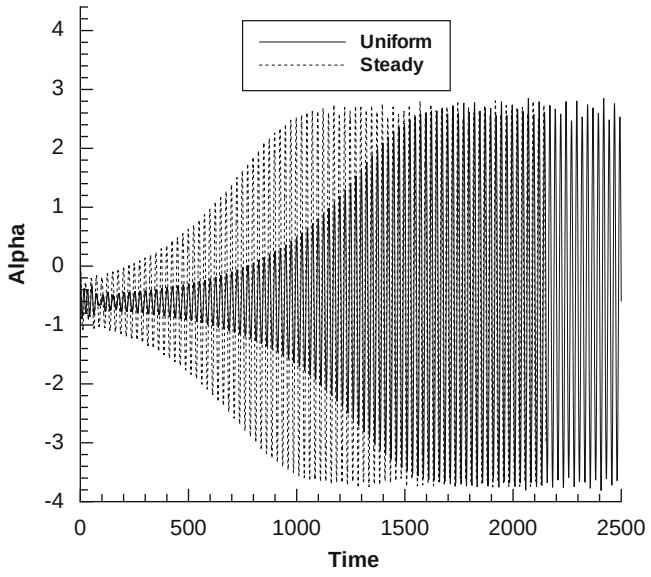

Fig. 8. Predicted pitch motion at M = 0.753, initial AoA = −0.45°.

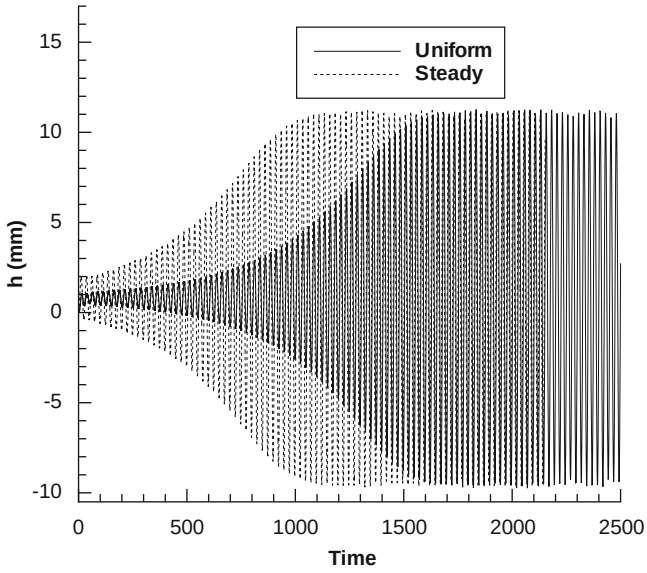

Fig. 9. Predicted plunge motion at M = 0.753, initial AoA = −0.45°.

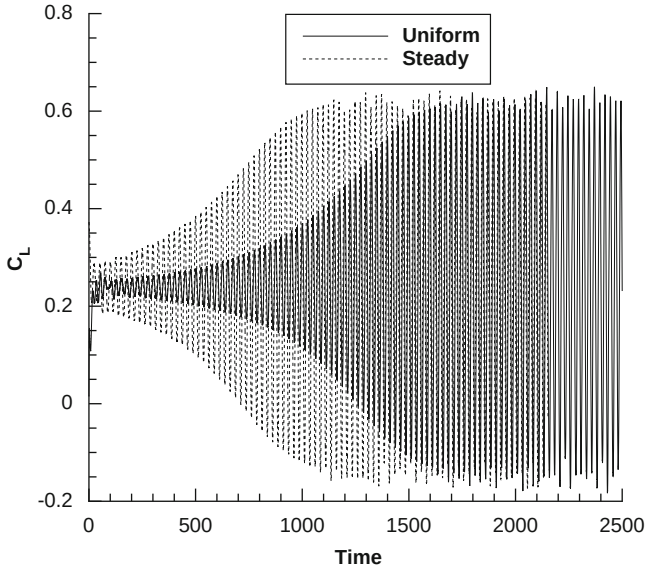

Fig. 10. Predicted lift coefficient at M = 0.753, initial AoA = −0.45°.

amplitudes even though the transition period is different. Figs. 10 and 11 plot the lift and moment coefficients, respectively.

The second series of LCO search use the procedure 2 at M = 0.753. The search for LCO is conducted by iterating α_0 and initial AoA to match the measured LCO amplitudes as close as possible.

Table 2 lists all the trail iteration cases at M = 0.753. Case A shows the computed results using procedure 1. Case B to F show the computed results with the initial field setup as uniform free stream at the different AoA and α_0 using procedure 2.

It can be seen from Table 2 that Case A matches the lift and moment coefficients best with the experiment among all the cases. However, the predicted LCO amplitudes are an order of magnitude higher than the experiment, just like all other cases.

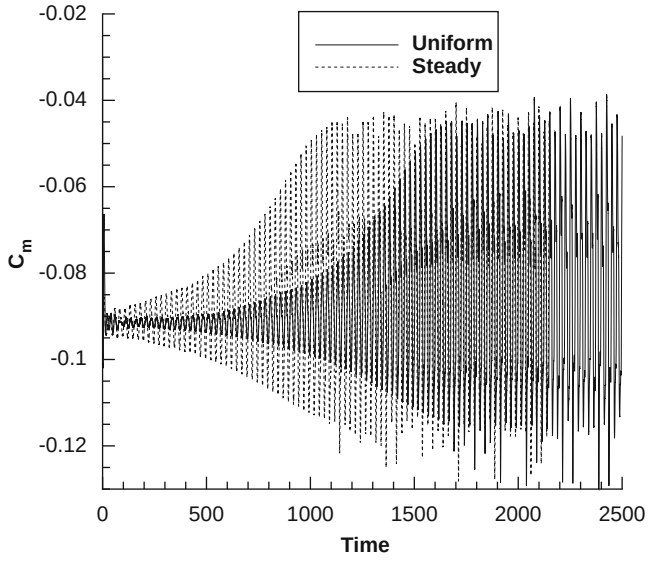

Fig. 11. Predicted moment coefficient at M = 0.753, initial AoA = −0.45°.

Table 2
Comparison of the test cases at M = 0.753.

NLR7301 LCO	Initial AoA	α_0°	Lift coef.	Moment coef.	h (mm)	α°	Frequency
Case A	0.0	0.25	0.2318	−0.0800	10.134	3.1942	33.49
Case B	0.0	0.60	0.2944	−0.0744	9.6768	2.9796	33.48
Case C	0.0	0.75	0.3180	−0.0756	8.6943	2.6921	33.48
Case D	0.0	0.85	0.3365	−0.0770	7.8386	2.4352	33.49
Case E	0.0	0.95	0.3548	−0.0790	6.9359	2.1566	33.48
Case F	0.05	0.85	0.3455	−0.0784	7.3517	2.2863	33.49
Experiment			0.272	−0.082	0.75	0.20	32.74

Table 3
Comparison of the test cases at M = 0.768.

NLR7301 LCO	Initial AoA	α_0°	Lift coef.	Moment coef.	h (mm)	α°	Frequency
Case A	0.0	0.68	0.2610	−0.0796	1.6509	0.4632	33.35
Case B	0.0	0.70	0.2758	−0.0807	4.2453	1.2349	33.36
Case C	0.0	0.75	0.2729	−0.0805	1.2617	0.3524	33.38
Case D	−0.033	0.75	0.2673	−0.0799	1.4351	0.4015	33.39
Case E	0.05	0.75	0.2803	−0.0816	0.8192	0.2287	33.36
Experiment			0.272	−0.082	0.75	0.20	32.74

Table 2 indicates that both the initial AoA and α_0 have influence on the amplitudes of LCO. However, the computation is not able to match the experimental amplitudes by adjusting AoA and α_0 due to the Mach number that is different from the experiment. The numerical simulation shows that the flow is separated at M = 0.753 with the large amplitude (Wang and Zha, 2009; Wang, 2009).

5.2.2.2. Mach number=0.768. Following procedure 2 developed in this paper, the LCO at the experimental Mach number of 0.768 is simulated. The dimensionless physical time step is the same as that used at M = 0.753.

Table 3 lists the iteration cases at Mach number 0.768. The computed averaged lift, moment coefficients, frequencies and amplitudes of Case E all agree excellently with the experiment. Figs. 12, 13, 14 and 15 show the computed LCO

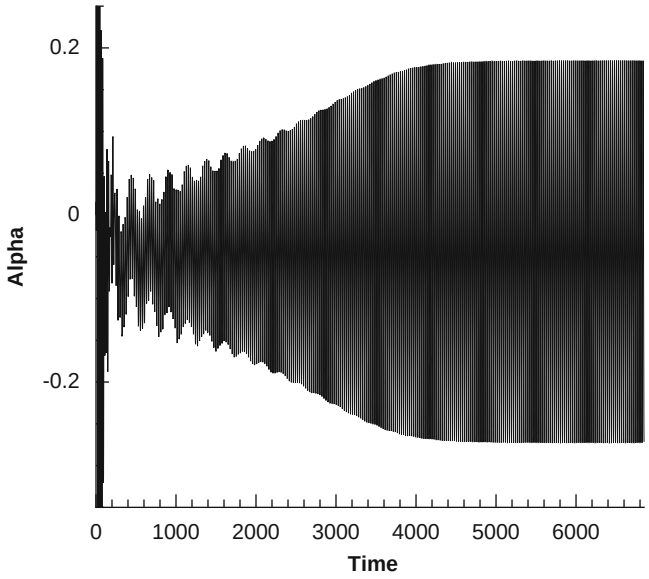

Fig. 12. Pitch motion predicted at M = 0.768.

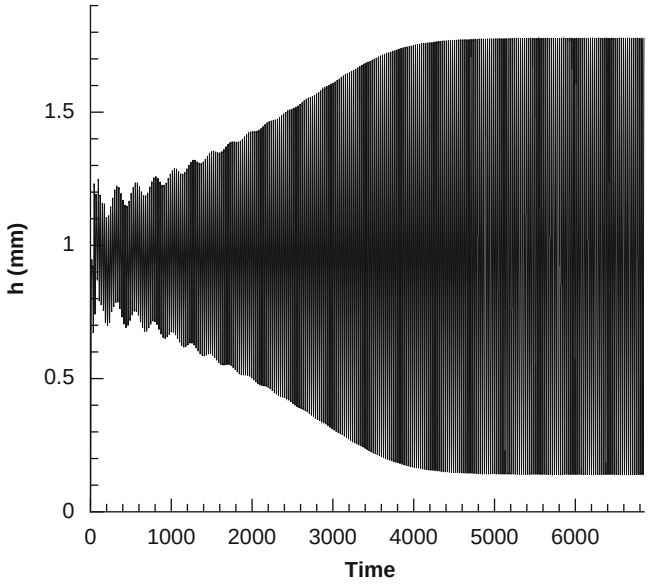

Fig. 13. Plunge motion predicted at M = 0.768.

amplitudes of pitch, plunge, lift and moment coefficient at Mach number 0.768 for Case E. Compared with results predicted at M = 0.753 as shown in Figs. 8, 9, 10 and 11, it can be seen that the predicted amplitudes at M = 0.768 are more than one order of magnitude smaller. This means that the Mach number has a significant effect on the amplitudes of plunge and pitching oscillation. The reason may be that the different Mach number causes different shock strength, different shock/boundary-layer interaction patterns and hence different unsteady nonlinear forcing and moment.

Totally 685 000 physical time steps are performed in the computation of case E with $t_c = 6850$. The stabilized LCO period in the simulation is up to $2250t_c$ and 88 cycles. The convergence history within a typical physical time step is shown in Fig. 16. It indicates that only about 7 pseudo time steps are needed to reach the convergence criteria of 10^{-6} in this computation. Fig. 17 shows the contours of Mach number at one cycle for case E. Figs. 18 and 19 plot the corresponding positions of (a)–(j) in a cycle for pitching and plunge movement, respectively. The computed phase

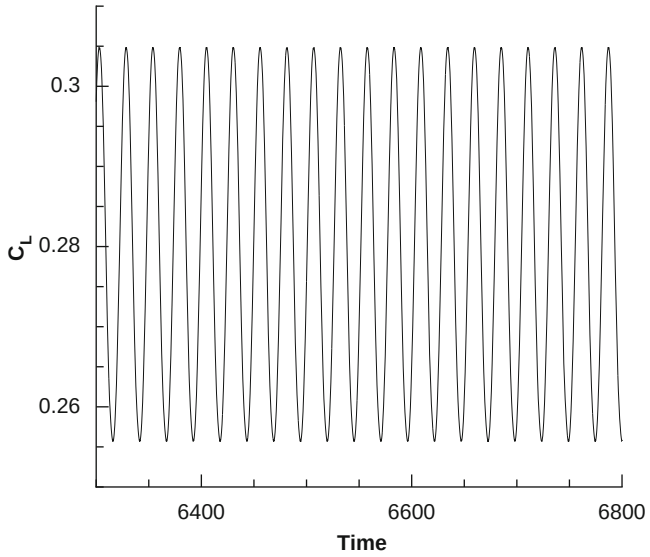

Fig. 14. Lift coefficient predicted at M = 0.768.

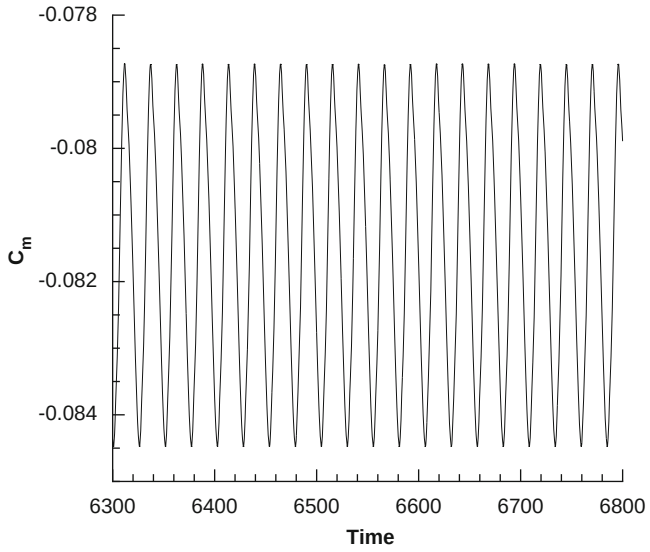

Fig. 15. Moment coefficient predicted at M = 0.768.

difference between pitching and plunge movement is 172°, which agrees very well with the experimental phase difference of 176°. Different from the LCO computation at M = 0.753 with a sizable separation, the computed separation at M = 0.768 is extremely small near the trailing edge, so small that it is not found when the streamlines are plotted for the first time. By zooming in the trailing edge region, the separation can be clearly seen as shown in Fig. 20. Fig. 21 plots the instantaneous surface pressure distributions at the two extreme α positions. On the pressure surface, the strength of the shock at the minimum α position is a little stronger than that at the maximum α position. There is a tiny shock motion on the pressure surface. On the suction surface, the strength of the shock at the maximum α position is stronger than that at the minimum α position. The shock oscillates back and forth slightly with the variation of AoA, and the amplitude is larger than that on the pressure surface. The computed results indicate that the LCO is maintained by the nonlinear forcing caused by shock oscillation and flow separation.

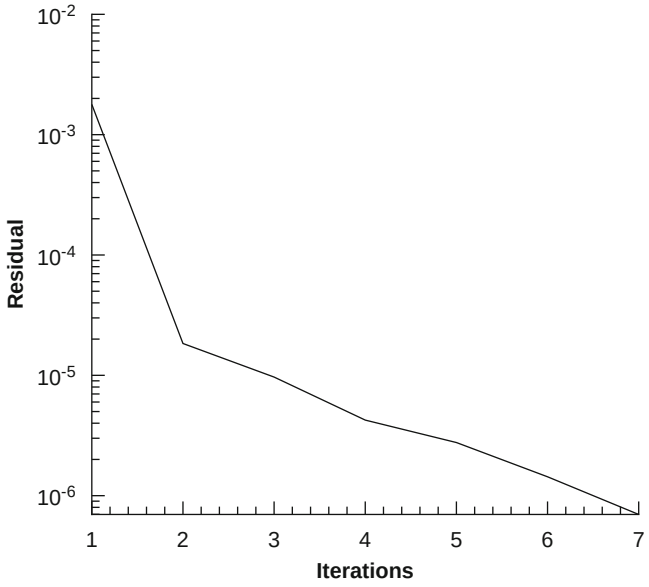

Fig. 16. Convergence history within a typical physical time step at M = 0.768.

Table 4 summarizes the computed LCO amplitudes and frequencies at different conditions compared with the experimental results (Schewe et al., 2003). At M = 0.753, the present computed results are comparable to those of Weber et al. (2001) and Tang et al. (2003). However, at M = 0.768 of the experimental condition, both the predicted plunge and pitching amplitudes agree excellently with the experiment, whereas the previous results predicted by other researchers (Weber et al., 2001; Tang et al., 2003) at M = 0.753 are more than one order of magnitude higher. This is the first time that a numerical simulation of NLR7301 airfoil LCO matches the experiment.

In general, the prediction accuracy of Case E at M = 0.768 is on the same order of the experiment measurement uncertainty. The only primary difference from the experiment for Case E is that the α_0 used in the simulation is 0.75°, whereas the experimental value is 1.9°. The α_0 only affects the initial moment imposed on the elastic system and remains as a constant in the whole LCO process. Such a difference may be attributed to uncertainties in the experiment and numerical simulation, and the sensitive nature of LCO to initial perturbations, which are difficult if not impossible to be made the same between the experiment and numerical simulation.

Note that the final LCO plunge amplitude is about 2.7/1000 of the chord length and the pitching amplitude is 0.2287°. These are very small values. The accurate resolution of such small scale vibration without it being damped out in the long time calculation may be attributed to the high-order low-diffusion numerical schemes and the fully coupled FSI model employed in this research.

An important phenomenon needs to be pointed out: that the LCO amplitudes are dependent on the initial flow fields. The results in Table 3 are computed using the initial field set equal to the uniform free-stream everywhere. If a converged steady state solution is used as the initial field, the LCO amplitudes may be very different with significantly greater magnitude. The different α_0 and initial AoA also set up the initial lift and moment to certain values. In other words, different initial perturbation may generate very different LCO solutions. This appears to be the bifurcation phenomenon due to the nonlinear aerodynamic loading of lift and moment, which are caused by the pattern of shock-wave/turbulent-boundary-layer interaction. If we can understand the systematic relationship between the LCO amplitude and initial perturbation, it may be possible to control the LCO and mitigate or prevent it. Even though the LCO amplitudes at different conditions vary significantly as presented in Tables 3 and 4, the computed frequencies vary little and agree well with the experimental value.

6. Conclusions

A fully coupled fluid–structure interaction with high order finite differencing schemes is conducted to investigate the flow nonlinearity of transonic NLR7301 airfoil LCO. The one equation Spalart–Allmaras RANS method with a low

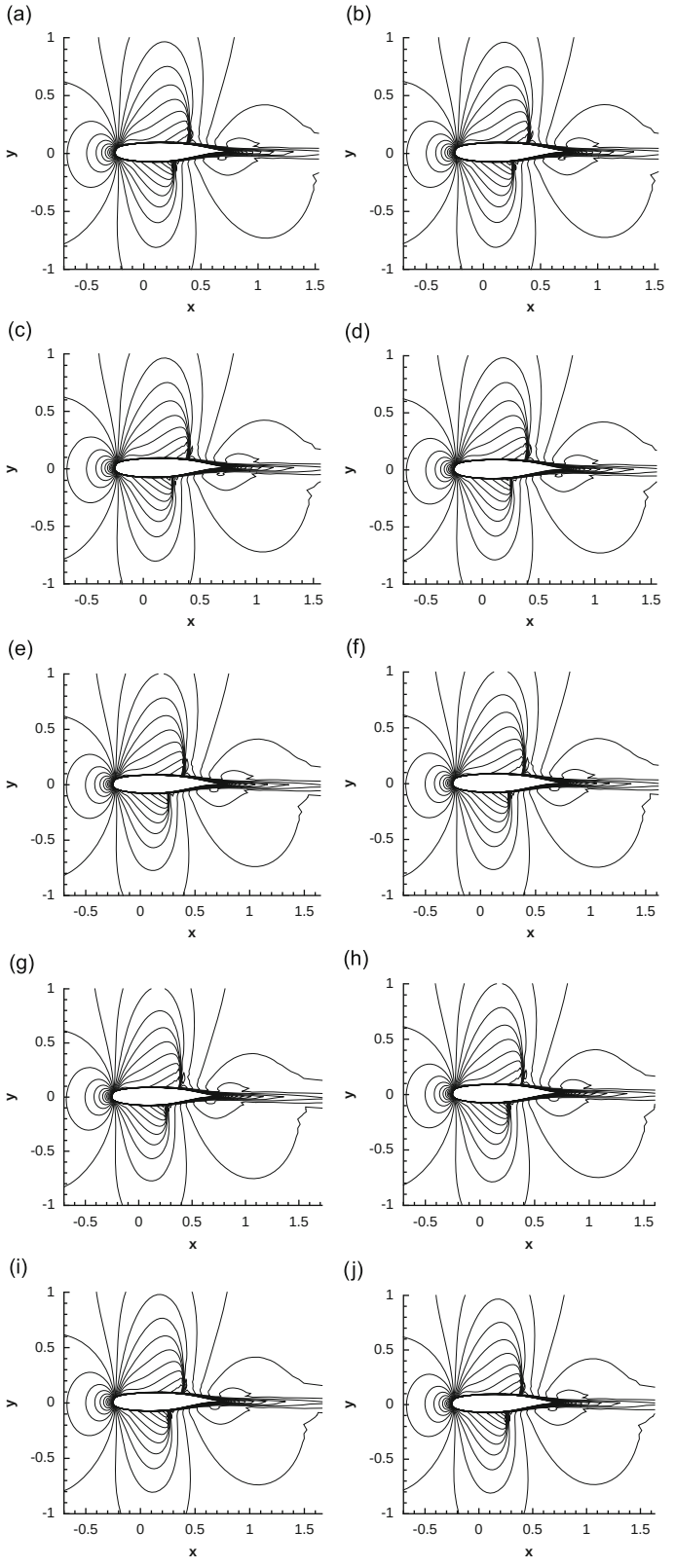

Fig. 17. Computed contours of Mach number at M = 0.768.

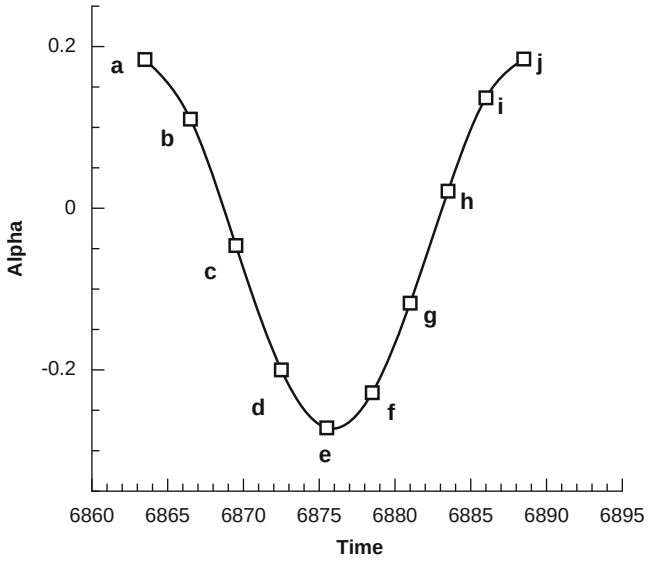

Fig. 18. Positions of pitching motion corresponding to Fig. 17.

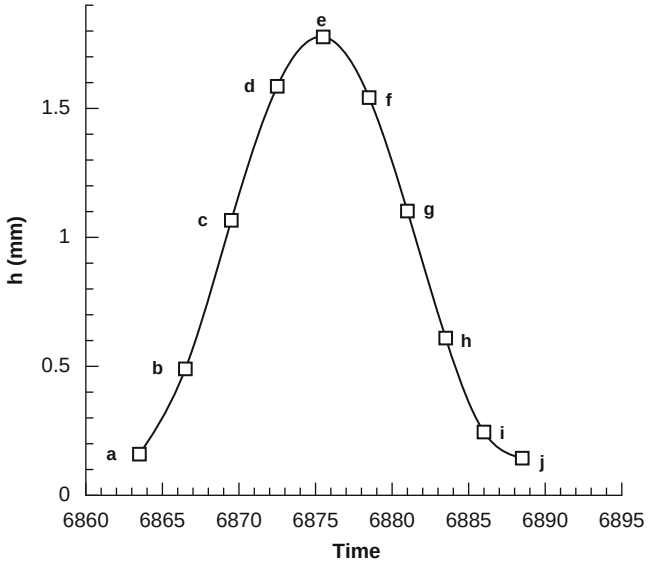

Fig. 19. Positions of plunge motion corresponding to Fig. 17.

diffusion E-CUSP scheme (Zha et al., 2008) and fifth-order WENO scheme for inviscid flux are employed. A fully conservative fourth-order central differencing scheme is used for the viscous terms.

At experimental Mach number of 0.768, the computed LCO amplitudes and frequency are in excellent agreement with experiment by adjusting AoA and α_0. The time averaged lift and moment coefficients also match the experiment very well. The free-stream Mach number has the major effect on the amplitudes of LCO due to different shock/boundary-layer interaction patterns. The initial flow field or initial perturbation has a strong influence on the amplitudes of LCO. The prediction accuracy is on the same order of the experiment measurement uncertainty. The only primary difference from the experiment is that the α_0 used in the simulation is 0.75°, whereas the experimental value is 1.9°. The α_0 only affects the initial moment imposed on the elastic system and remains as a constant in the whole LCO process. Such a difference may be attributed to the uncertainities in the experiment and numerical simulation, and the sensitive nature of LCO to initial perturbations, which are difficult if not impossible to be matched exactly.

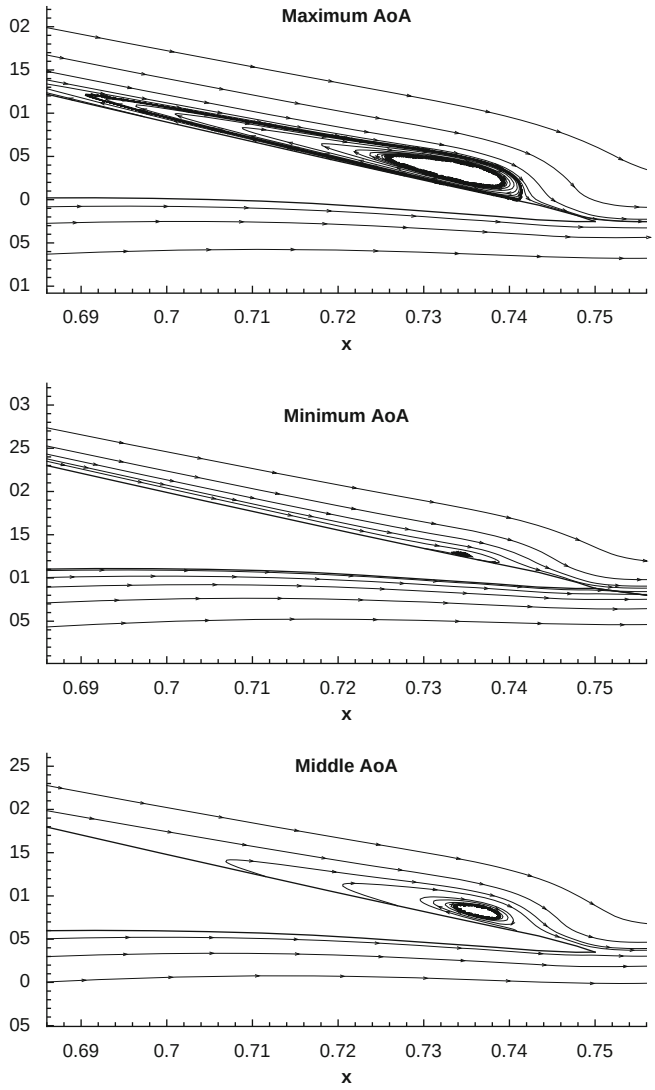

Fig. 20. Stream line for Case E at M = 0.768 showing no flow separation due to shock/boundary layer interaction.

This research appears to be the first in which a numerical simulation of NLR7301 airfoil LCO matches the experiment. It may be attributed to the high-order low-diffusion numerical schemes, the fully coupled FSI model, and the turbulence model used in this research.

The simulations in this paper also confirm some of the experimental observations and answer some important questions. First, the LCOs with relatively small amplitude are captured with unbounded flows in the numerical simulation. This means they should not be the artifacts of the wind-tunnel experiment and most likely are a factual phenomenon. Second, the co-existence of multiple LCOs at constant flow conditions is confirmed in our simulation. The reason that other numerical simulations only capture the LCOs with large amplitudes may be due to their high numerical dissipation that either smears out the small amplitude LCO or is only able to resolve the large amplitude LCOs. Third, the numerical simulation of this research confirms that the wall boundary layer transition from laminar to turbulent does not have a large effect on LCOs at high Reynolds number, because our simulation assumes that the boundary layer is fully turbulent from the airfoil leading edge. Fourth, the simulation confirms that the wind tunnel wall interference with or without a perforated test-section does not have much effect on LCOs because the present simulation uses the unbounded flow condition with no wind tunnel wall effect at all. Fifth, the numerically captured LCO at M = 0.768 is accompanied by flow separation, although the separation region is very small. This verifies the

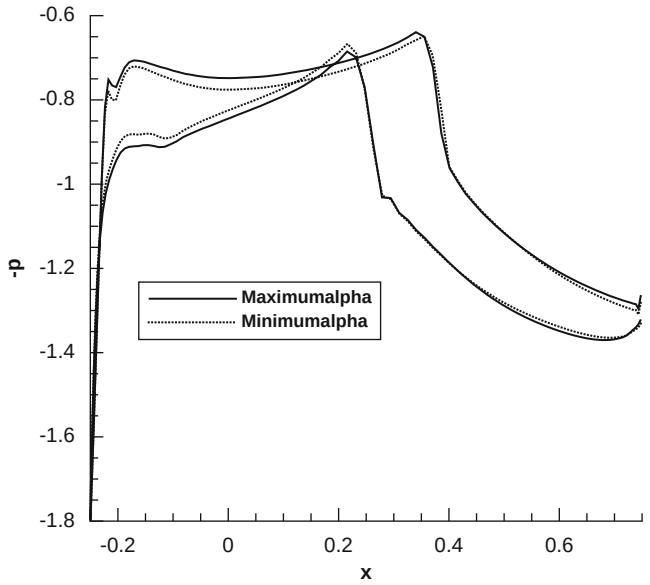

Fig. 21. Pressure distributions at extreme α positions corresponding to Fig. 17.

Table 4
LCO comparison of computation and experiment.

NLR7301 LCO	Mach	h (mm)	Error (mm)	α°	Error	f (Hz)	Error (Hz)
Present	0.768	0.8192	0.069	0.2287°	0.0287°	33.36	0.62
Present	0.753	10.134	9.384	3.1942°	2.9942°	33.49	0.75
Weber et al. (2001)	0.753	10.5	9.75	4.09°	3.89°	33.42	0.68
Tang et al. (2003)	0.753	8.99	8.24	3.17°	2.97°	34.3	1.56
Experiment	0.768	0.75		0.20°		32.74	

hypothesis that the LCO processes are maintained by the nonlinearity of flow separation induced by shock/boundary-layer interaction.

Acknowledgment

This work is supported by (US) Air Force Office of Scientific Research Grant FA9550-06-1-0198 monitored by Fariba Fahroo. The discussion with Dr Philip Beran at (US) Air Force Research Lab is greatly appreciated.

References

Bendiksen, O.O., 1992. Role of shock dynamics in transonic flutter. AIAA Paper 92-2121.

Bendiksen, O.O., Seber, G., 2008. Fluid–structure interactions with both structural and fluid nonlinearities. Journal of Sound and Vibration 315, 664–684.

Castro, B., Ekaterinaris, J.A., Platzer, M.F., 2001. Analysis of the effect of propous wall interference on transonic airfoil flutter. AIAA Paper 2001-2725.

Chen, X.-Y., Zha, G.-C., 2005. Fully coupled fluid–structural interactions using an efficient high resolution upwind scheme. Journal of Fluids and Structures 20, 1105–1125.

Chen, X.-Y., Zha, G.-C., Hu, Z.-J., 2004. Numerical simulation of flow induced vibration based on fully coupled-structural interactions. In: AIAA 34th AIAA Fluid Dynamics Conference, AIAA Paper 2004-2240.

Chen, X.-Y., Zha, G.-C., Yang, M.-T., 2007. Numerical simulation of 3-d wing flutter with fully coupled fluid–structural interaction. Journal of Computers & Fluids 36, 856–867.

Davis, S.S., 1982. NACA 64 A010 (NACA Ames Model) oscillatory pitching. Technical Report AGARD, Report No. 702, AGARD.
Dietz, G., Schewe, G., Mai, H., 2004. Experiments on heave/pitch limit-cycle oscillations of a supercritical airfoil close to the transonic dip. Journal of Fluids and Structures 19, 1–16.
Gordnier, R.E., 2003. Computation of limit-cycle oscillations of a delta wing. Journal of Aircraft 40, 1206–1208.
Jameson, A., 1991. Time dependent calculations using multigrid with applications to unsteady flows past airfoils and wings. AIAA Paper 91-1596.
McMullen, M., Jameson, A., Alonso, J., 2002. Application of a nonlinear frequency domain solver to the euler and Navier–Stokes equations. AIAA Paper-2002-0120.
Morton, S., Beran, P.S., 1999. Hopf-bifurcation analysis of airfoil flutter at transonic speeds. Journal of Aircraft 36, 421–429.
Schewe, G., Knipfer, A., Mai, H., Dietz, G., 2002. Experimental and numerical investigation of nonlinear effects in transonic flutter. DLR report: DLR IB 232-2002 J01.
Schewe, G., Mai, H., Dietz, G., 2003. Nonlinear effects in transonic flutter with emphasis on manifestations of limit cycle oscillation. Journal of Fluids and Structures 18, 3–22.
Shen, Y.-Q., Wang, B.-Y., Zha, G.-C., 2007. Implicit weno scheme and high order viscous formulas for compressible flows. AIAA Paper 2007-4431.
Shen, Y.-Q., Zha, G.-C., Chen, X., 2008. High order conservative differencing for viscous terms and the application to vortex-induced vibration flows. In: 38th AIAA Fluid Dynamics Conference and Exhibit, AIAA Paper 2008-4059, Seattle, WA, USA.
Shen, Y.-Q., Zha, G.-C., Wang, B.-Y., 2009. Improvement of stability and accuracy for weighted essentially nonoscillatory scheme. AIAA Journal 47, 331–344.
Shu, C.-W., 1997. Essentially non-oscillatory and weighted essentially non-oscillatory schemes for hyperbolic conservation laws. NASA /CR-97-206253, ICASE Report no. 97-65.
Spalart, P., Allmaras, S., 1992. A one-equation turbulence model for aerodynamic flows. AIAA-92-0439.
Tang, L., Bartels, R.E., Chen, P.-C., Liu, D.D., 2003. Numerical investigation of transonic limit cycle oscillations of a two-dimensional supercritical wing. Journal of Fluids and Structures 17, 29–41.
Wang, B.-Y., 2009. Detached-eddy simulation of flow non-linearity of fluid–structural interactions using high order schemes and parallel computation. Ph.D. Thesis, University of Miami, FL, USA.
Wang, B.-Y., Zha, G.-C., 2008a. Comparison of a low diffusion e-cusp and the roe scheme for rans calculation. 46th AIAA Aerospace Sciences Meeting and Exhibit, AIAA Paper 2008-0596.
Wang, B.-Y., Zha, G.-C., 2008b. A general sub-domain boundary mapping procedure for structured grid cfd parallel computation. AIAA Journal of Aerospace Computing, Information, and Communication 5, 425–447.
Wang, B.-Y., Zha, G.-C., 2009. Dettached Eddy Simulation of transonic airfoil limited cycle oscillation with high order WENO scheme. The 47th AIAA Aerospace Sciences Meeting and Exhibit, AIAA Paper 2009-1507, Orlando, Florida.
Weber, S., Jones, K.D., Ekaterinaris, J.A., Platzer, M.F., 2001. Transonic flutter computations for the nlr 7301 supercritical airfoil. Aerospace Science and Technology 5, 293–304.
Zha, G.-C., Shen, Y.-Q., Wang, B.-Y., 2008. Calculation of Transonic Flows Using WENO Method with a Low Diffusion E-CUSP Upwind Scheme. 46th AIAA Aerospace Sciences Meeting, AIAA Paper 2008-0745, Reno, NV, USA.